Superlens Enhanced 2-D Microwave Tomography With Contrast Source Inversion Method

ANTON MENSHOV[1] (Member, IEEE), AND VLADIMIR I. OKHMATOVSKI [2] (Senior Member, IEEE)

[1]CEMWorks, Inc., Winnipeg, MB R3B 0P4, Canada

[2]Department of Electrical and Computer Engineering, University of Manitoba, Winnipeg, MB R3T 5V6, Canada

CORRESPONDING AUTHOR: V. I. OKHMATOVSKI (e-mail: vladimir.okhmatovski@umanitoba.ca)

ABSTRACT The contrast source inversion (CSI) algorithm is one of the primary techniques used for solution of non-linear inverse problems in microwave tomography. In this paper, we describe a modification of the CSI method adapted to imaging of the 2-D objects in the presence of the focusing media under TM-polarization. The focusing media is presented in the form of the Veselago lens. The data domain and imaging domain are properly positioned with respect to the location of the lens. Specifically, the sensors are located at the focal points of the lens with respect to the location of the individual pixels discretizing the contrast source. Such positioning of the source and observation locations in the presence of the lens, eliminates rank deficiency in the formulation of the inverse problem and results in significant improvements to both convergence speed of underlying conjugate gradient iterations and the accuracy of the image reconstruction in the CSI method.

INDEX TERMS Microwave tomography, contrast source inversion, microwave imaging, inverse problem, focusing media, conjugate gradient.

I. INTRODUCTION

MICROWAVE Tomography (MWT) has various important applications in medical imaging [1], nondestructive testing [2], security screening [3], structural health monitoring [4], remote sensing [5], and other areas [6]. While qualitative imaging techniques [7], such as Ground Penetrating Radar [8] and Synthetic Aperture Radar [9] methods, have been well developed and can often provide useful information about the location and shape of the imaged objects, it is the more accurate quantitative methods which have a potential to greatly expand the areas of MWT applicability. The quantitative methods of MWT solve the non-linear inverse problem of reconstructing electric permittivity and magnetic permeability of the objects from the information on how the object scatters the electromagnetic fields. The two primary methods of quantitative MWT are the CSI method [10] and the Distorted Born Iterative Method (DBIM) [11] (a.k.a. Gauss-Newton Inversion (GNI) method [19]). Both methods are iterative in nature and provide about equal abilities in quality of reconstruction and the overall computational cost [12], [13].

The CSI method, however, is much easier to implement as it does not require inversion of either the forward or inverse scattering operators at each iteration of the underlying non-linear optimization scheme (Conjugate-Gradient (CG) method in CSI and Gauss-Newton method in DBIM). The CSI method also offers a great flexibility in accounting for the complex media in which the imaging experiments are conducted. This method has been used for imaging of the objects in both free-space environment [14] and metal enclosures [15]. The latter has been shown to improve the quality of the CSI images through the modification of the non-symmetric enclosure positioning with respect to the imaged objects and hence producing a broader variety in the scattered field information.

The discretized inverse scattering operators, i.e., the operators mapping the scattered field to the contrast sources producing them, most commonly have incomplete rank [16]. Inversion of such operators in MWT presents an ill-posed problem [17] which does not have a unique solution unless the problem is regularized [18]. Typically, the regularization is done mathematically through augmentation of the

inverse scattering operators with additional constraints of a non-Maxwellian nature (e.g., the boundedness of the solution in Tikhonov regularization [19]). In [20], [21], it was shown, however, that the rank-deficiency of the discretized inverse scattering operator and thus the ill-posedness of the inverse scattering problem can be eliminated in rigorous compliance with Maxwell's Equations. For that purpose, the kernel of the forward scattering operator must be the Green's function of a focusing media and the sensor positions must be properly situated with respect to the locations of the sources in the imaging domain. Under these conditions, the inverse scattering problem can be solved in the same rigorous manner as the forward scattering problem.

In this paper, we study how the elimination of rank deficiency in the discretized inverse scattering operator established through staging of the imaging experiment in appropriate focusing media impacts the performance of the CSI method. As the focusing media, we use the idealized model of the Veselago lens [22], [23]. The lens is formed by a dielectric slab of double negative parameters, finite thickness, and infinite extent. Such lens, upon both the values of relative permittivity and permeability approaching negative unity, has the ability to reconstruct at its focal point both evanescent and propagating waves contained in the spectrum of the point source [24]. Such superlenses [25] have been experimentally demonstrated both in microwave [26] and optical regimes [27]. As a result, the Green's function of the lens has singular behavior at the location of the source point and near singular behavior at the corresponding focal point. We position the pixelated imaging domain (imaging domain discretized with piece-wise basis functions) on one side of the lens, while sampling the scattered field on the other side of the lens at the locations symmetrically corresponding to the centers of the object pixels. Under these conditions and sufficient focusing established by the lens, the discretized inverse scattering operator can be shown to attain its full rank. We subsequently perform the full non-linear inversion using CSI algorithm that is appropriately modified to account for the presence of the lens. Since the functional which is minimized in the CSI method is constructed via Fréchet derivatives [28] taken with respect to the contrast source function, the rigorous modification of the CSI method accounting for the presence of focusing media is effected through the use of the lens Green's function in the forward and inverse scattering operators instead of the homogeneous background Green's function featured in the conventional CSI algorithm.

The numerical results show that performing non-linear inversion with the CSI method in the focusing media instead of the conventional non-focusing media [12], [14], [29], substantially improves the accuracy of the image reconstruction. The new CSI algorithm is shown to be more robust also. It exhibits consistent convergence to an accurate image of the object within a single frequency experiment and regardless of the object shape. To validate the CSI algorithm and study it's

properties the 'E'-shaped and 2-layer square inhomogeneous objects are considered.

II. CONTRAST SOURCE INVERSION METHOD IN FOCUSING MEDIA
A. FORMULATION
Consider TM_z polarized time-harmonic scattering (in $e^{i\omega t}$ time convention) in 2-D from a non-magnetic dielectric cylinder occupying cross-sectional area D, oriented along z-axis, and having arbitrary cross-section and spatial distribution of complex relative dielectric permittivity $\epsilon(\boldsymbol{\rho}')$. We will define the contrast $\chi(\boldsymbol{\rho}')$ and contrast source $w(\boldsymbol{\rho}')$ functions, as follows:

$$\chi(\boldsymbol{\rho}') = \frac{k^2(\boldsymbol{\rho}') - k_b^2(\boldsymbol{\rho}')}{k_0^2} = \epsilon(\boldsymbol{\rho}') - \epsilon_b(\boldsymbol{\rho}'),$$
$$w(\boldsymbol{\rho}') = \chi(\boldsymbol{\rho}')E(\boldsymbol{\rho}'), \tag{1}$$

where $\boldsymbol{\rho}'$ is the position vector, $E(\boldsymbol{\rho}') = E(\boldsymbol{\rho}')\hat{z}$ is the total electric field, $k_0 = \omega\sqrt{\varepsilon_0\mu_0}$, $k_b(\boldsymbol{\rho}') = \omega\sqrt{\epsilon_b(\boldsymbol{\rho}')\varepsilon_0\mu_0}$, and $k(\boldsymbol{\rho}') = \omega\sqrt{\epsilon(\boldsymbol{\rho}')\varepsilon_0\mu_0}$ are the wavenumber of free-space, background media and dielectric cylinder, respectively. Note, that $\chi(\boldsymbol{\rho}') \neq 0$ only when $\boldsymbol{\rho}' \in D$.

We can formulate the forward and inverse scattering problems using the following operator notation:

$$\mathcal{G}^{\mathcal{A}}\{\boldsymbol{\rho}, w\} = k_0^2 \iint_{\mathcal{D}} ds' w(\boldsymbol{\rho}')G(\boldsymbol{\rho}, \boldsymbol{\rho}'), \quad \boldsymbol{\rho} \in \mathcal{A}, \tag{2}$$

where $\mathcal{A}$ is the domain where the position vector $\boldsymbol{\rho}$ resides, $\boldsymbol{\rho}$ and $\boldsymbol{\rho}'$ are the observation and source points, respectively, and $G(\boldsymbol{\rho}, \boldsymbol{\rho}')$ is 2-D Green's function satisfying

$$\nabla^2 G(\boldsymbol{\rho}, \boldsymbol{\rho}') + k_b^2(\boldsymbol{\rho}')G(\boldsymbol{\rho}, \boldsymbol{\rho}') = -\delta(\boldsymbol{\rho} - \boldsymbol{\rho}'). \tag{3}$$

Thus, by virtue of (2) we can define operator $\mathcal{G}^{\mathcal{S}} : \mathcal{D} \mapsto \mathcal{S}$ producing the scattered electric field at sensor locations $\mathcal{S}$ due to contrast sources w inside the imaging domain $\mathcal{D}$ enclosing cylinder area D and operator $\mathcal{G}^{\mathcal{D}} : \mathcal{D} \mapsto \mathcal{D}$ producing the scattered electric field at the imaging domain $\mathcal{D}$ due to contrast sources w in it.

If the dielectric permittivity distribution $\epsilon(\boldsymbol{\rho}')$ is known, then the forward scattering problem can be formulated, as follows:

$$E^{\mathrm{sc}}(\boldsymbol{\rho}) = E(\boldsymbol{\rho}) - E^{\mathrm{in}}(\boldsymbol{\rho}) = \mathcal{G}^{\mathcal{D}}\{\boldsymbol{\rho}, \chi(\boldsymbol{\rho}')E(\boldsymbol{\rho}')\},$$
$$\boldsymbol{\rho}, \boldsymbol{\rho}' \in D, \tag{4}$$

where $\chi(\boldsymbol{\rho}')$ is a known contrast function and $E(\boldsymbol{\rho}')$ is an unknown field due to this contrast in imaging domain $\boldsymbol{\rho}' \in D$. Similarly, inverse scattering problem is given by

$$E^{\mathrm{sc}}(\boldsymbol{\rho}) = \mathcal{G}^{\mathcal{S}}\{\boldsymbol{\rho}, \chi(\boldsymbol{\rho}')E(\boldsymbol{\rho}')\} = \mathcal{G}^{\mathcal{S}}\{\boldsymbol{\rho}, w(\boldsymbol{\rho}')\},$$
$$\boldsymbol{\rho} \in \mathcal{S}, \boldsymbol{\rho}' \in \mathcal{D}, \tag{5}$$

where both contrast function $\chi(\boldsymbol{\rho}')$ and field inside the scatterer $E(\boldsymbol{\rho}')$ are unknown, while $E^{\mathrm{sc}}(\boldsymbol{\rho}), \boldsymbol{\rho} \in \mathcal{S}$ is known. It is common to refer to the problem of finding the contrast function $\chi(\boldsymbol{\rho}')$ as *inverse scattering problem* and the
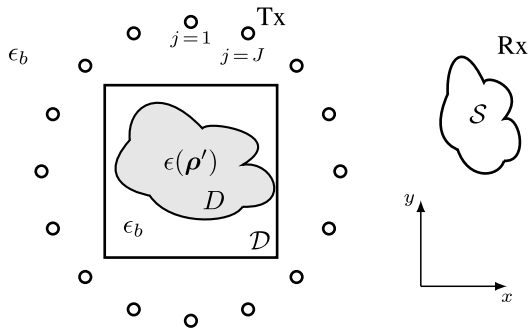
FIGURE 1. Inverse problem configuration. The 2-D dielectric cylinder occupying cross-sectional area *D* is illuminated by *J* sources (Tx) and the scattered field is collected at the sensors (Rx) residing in $\mathcal{S}$. The contrast and contrast source functions defined in (1) are reconstructed inside the imaging domain $\mathcal{D}$.

problem of finding the contrast sources $w(\rho')$ as *inverse source problem* [19].

A typical set up for a solution of the inverse problem is depicted in Fig. 1. The scattered field data E^{sc} is collected at the sensors residing in the domain $\mathcal{S}$ for J excitations that illuminate the object by different source configuration. In general, the imaging domain $\mathcal{D}$ is different from the object domain D since the exact size and shape of the imaging object are unknown and are subject of reconstruction.

Forward scattering problem (4) is in a form of a second-kind Fredholm [30] integral equation and, therefore, it is well-posed. However, if all sensors are located outside the imaging domain $\mathcal{D} \bigcap \mathcal{S} = \emptyset$ (non-invasive imaging procedure), the inverse source problem (5) is in the form of the first-kind Fredholm integral equation with smooth kernel which makes it ill-posed.

B. GREEN'S FUNCTION OF VESELAGO LENS

Veselago lens has a unique property of reassembling at the focal point not only the propagating waves as the conventional lenses do [30] but also the evanescent waves [22], [23]. The evanescent waves while traveling through the lens acquire the same gain as their attenuation in the process of propagation outside the lens, hence, arriving to the focal point with their initial magnitude with which they depart from the source point. Depiction of the field produced by a point source in the presence of the Veselago lens computed with *OpenFMM* software [31] is shown in Fig. 2. Besides the singular field behavior in the vicinity of the source point location, one can see two focal points corresponding to the points of ray intersection (Fig. 3). One focal point is located half way through the lens' thickness and the other one is on the opposite side of the lens symmetrically situated with respect to the center of the lens and the location of the source point.

The operator definition (2) can be rewritten for the imaging experiment scenario in the presence of the Veselago lens (or any other focusing media), as follows:

$$\mathcal{F}^{\mathcal{A}}\{\rho, w\} = k_0^2 \iint_{\mathcal{D}} ds' w(\rho') G^{\text{foc}}(\rho, \rho'), \quad \rho \in \mathcal{A}, \quad (6)$$
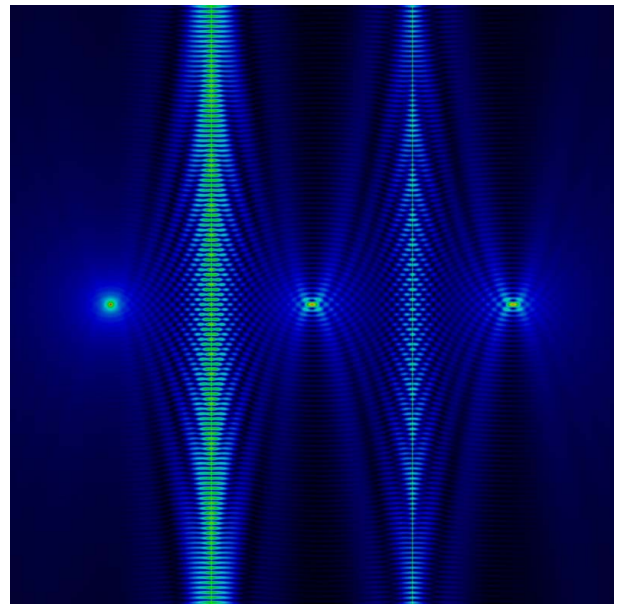

FIGURE 2. Electric field intensity produced by point source located 2 m away from the surface the Veselago lens (computed with *OpenFMM* [31]). The lens is modelled by a 4 m thick and 40 m wide slab, having $\varepsilon_r = -1.00001$ and $\mu_r = -1$. The source is operating at 1.5 GHz frequency in vacuum $\epsilon_b = \varepsilon_0$.

where $G^{\text{foc}}(\rho, \rho')$ is the Green's function of the focusing media [22], [32], and $\mathcal{A}$ is the domain where the position vector to the observation point ρ resides. Thus, we can define an operator $\mathcal{F}^{\mathcal{S}} : \mathcal{D} \mapsto \mathcal{S}$ producing the scattered electric field at sensor locations $\mathcal{S}$ due to contrast sources w inside the imaging domain $\mathcal{D}$ inclosing cylinder area D and an operator $\mathcal{F}^{\mathcal{D}} : \mathcal{D} \mapsto \mathcal{D}$ producing the scattered electric field in the imaging domain $\mathcal{D}$ due to contrast sources w. Sensors have to be located inside the focal point of the lens to allow for the efficient inversion. In this work, the Green's function of the Veselago lens was computed directly via error-controlled evaluation of Sommerfeld integrals [32].

C. DISCRETIZATION

The Method of Moments (MoM) discretization of the operators $\mathcal{G}^{\mathcal{S}}$ and $\mathcal{G}^{\mathcal{D}}$ given in (2) or their focusing media counterparts $\mathcal{F}^{\mathcal{S}}$ and $\mathcal{F}^{\mathcal{D}}$ given in (6) requires the discretization of the imaging domain $\mathcal{D}$ and sensor domain $\mathcal{S}$. The domain $\mathcal{S}$ is naturally discrete as the scattered field is observed at a finite number of sensors K. The position of the kth sensor is defined by the radius vector κ_k, $k = 1, \ldots, K$. The imaging domain $\mathcal{D}$ is discretized with M square cells and the position of the mth cell centroid is defined by the radius-vector $\rho_{m'}$.

The unknown contrast sources $w(\rho')$ are discretized by using piece-wise basis functions [33]

$$w(\rho') \cong \sum_{m'=1}^{M} w_{m'} p_{m'}(\rho'),$$

$$p_{m'}(\rho') = \begin{cases} 1, & \rho' \in S_{m'} \\ 0, & \rho' \notin S_{m'} \end{cases} \quad (7)$$
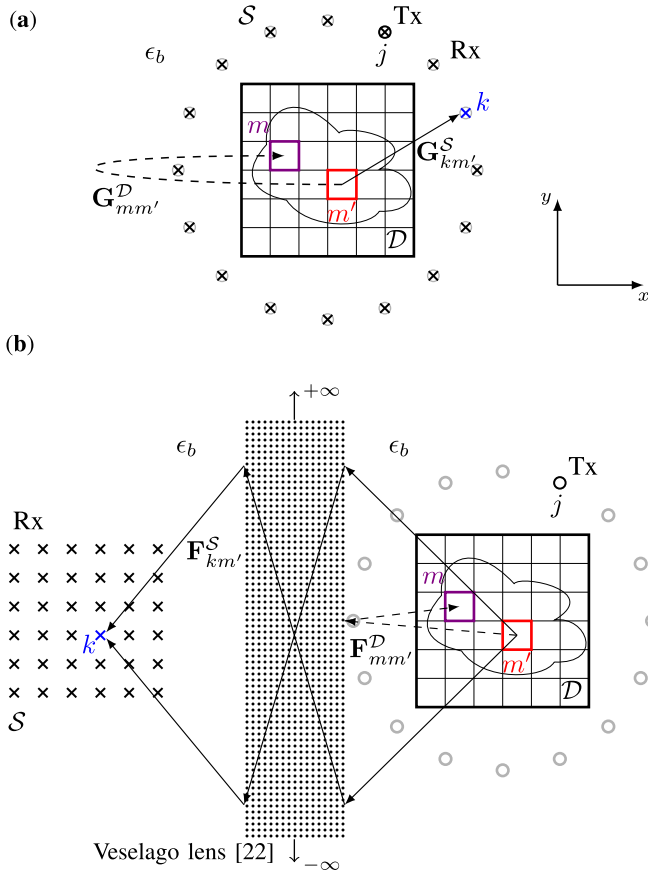
FIGURE 3. (a) Discretized operators $\mathbf{G}^{\mathcal{S}}$ (11) and $\mathbf{G}^{\mathcal{D}}$ (10) acting on the contrast source $w_{m'}$ produce the scattered field at the kth sensor in $\mathcal{S}$ and mth pixel in $\mathcal{D}$, respectively, for the jth excitation of the imaging experiment staged in the non-focusing media. (b) Discretized operators $\mathbf{F}^{\mathcal{S}}$ (13) and $\mathbf{F}^{\mathcal{D}}$ (12) acting on the contrast source $w_{m'}$ produce the scattered field at the kth sensor in $\mathcal{S}$ and mth pixel in $\mathcal{D}$, respectively, for the jth excitation of the imaging experiment staged in the presence of the lens.

with $S_{m'}$ being the m'th cell element in $\mathcal{D}$. The ranges of the operators $\mathcal{G}^{\mathcal{D}}$ and $\mathcal{G}^{\mathcal{S}}$ (2) are tested with delta-functions t_m positioned at the centroids of the mesh elements and delta-functions τ_k positioned at the sensor locations, respectively

$$t_m(\boldsymbol{\rho}) = \delta(\boldsymbol{\rho} - \boldsymbol{\rho}_m),$$
$$\tau_k(\boldsymbol{\rho}) = \delta(\boldsymbol{\rho} - \boldsymbol{\kappa}_k). \tag{8}$$

Thus, substitution of (7) into (2), followed by point-sampling of the scattered field in the ranges of the operators $\mathcal{G}^{\mathcal{D}}$ and $\mathcal{G}^{\mathcal{S}}$ casts (2) in the matrix form

$$\underline{E}^{\mathrm{sc},\mathcal{D}} = \mathbf{G}^{\mathcal{D}} \cdot \underline{w}, \quad \underline{E}^{\mathrm{sc},\mathcal{S}} = \mathbf{G}^{\mathcal{S}} \cdot \underline{w}, \tag{9}$$

where $\underline{w}$ is an $M \times 1$ vector of unknown contrast source expansion coefficients in (7), $\underline{E}^{\mathrm{sc},\mathcal{D}}$ is an $M \times 1$ vector of values of the scattered field at M centroids of the cells discretizing the imaging domain $\mathcal{D}$, $\underline{E}^{\mathrm{sc},\mathcal{S}}$ is an $K \times 1$ vector of values of the scattered field at K sensor locations, and matrix elements of $\mathbf{G}^{\mathcal{D}}$ and $\mathbf{G}^{\mathcal{S}}$ are the inner products [33]

$$\mathbf{G}^{\mathcal{D}}_{m,m'} = \left\langle t_m, \mathcal{G}^{\mathcal{D}} \circ p_{m'} \right\rangle, \tag{10}$$

$$\mathbf{G}^{\mathcal{S}}_{k,m'} = \left\langle \tau_k, \mathcal{G}^{\mathcal{S}} \circ p_{m'} \right\rangle, \tag{11}$$

where $m, m' = 1, \ldots, M$, and $k = 1, \ldots, K$.

Similarly, point-sampling of the scattered field in the ranges of the focused media operators $\mathcal{F}^{\mathcal{D}}$ and $\mathcal{F}^{\mathcal{S}}$ results in their discretized forms $\mathbf{F}^{\mathcal{D}}$ and $\mathbf{F}^{\mathcal{S}}$, and the matrix entries are defined as inner products

$$\mathbf{F}^{\mathcal{D}}_{m,m'} = \left\langle t_m, \mathcal{F}^{\mathcal{D}} \circ p_{m'} \right\rangle, \tag{12}$$

$$\mathbf{F}^{\mathcal{S}}_{k,m'} = \left\langle \tau_k, \mathcal{F}^{\mathcal{S}} \circ p_{m'} \right\rangle, \tag{13}$$

where $m, m' = 1, \ldots, M$, and $k = 1, \ldots, K$. A general example of the operators $\mathbf{G}^{\mathcal{S}}$ and $\mathbf{F}^{\mathcal{S}}$ in the inverse problem setup is depicted in Fig. 3.

The evaluation of the integrals in (10)–(13) can be done using standard Gauss-Legendre quadrature rules [34] after the singularity is extracted and evaluated analytically using the technique in [35].

D. $\mathcal{G}^{\mathcal{S}}$ AND $\mathcal{F}^{\mathcal{S}}$ OPERATORS

The nearly singular field at the focal point is the key to elimination of the rank deficiency in the operator $\mathcal{F}^{\mathcal{S}}$ producing the scattered field at sensor locations, provided each kth sensor position (defined by $\boldsymbol{\kappa}_k$) is situated at the focal point of the mth pixel center $\boldsymbol{\rho}_m$ with respect to the lens' center, as shown in Fig. 3. Under such particular selection of the sensor locations and the corresponding discretization of the imaging domain, the matrix $\mathbf{F}^{\mathcal{S}}$ of the discretized operator $\mathcal{F}_{\mathcal{S}}$ becomes diagonally dominant, as the contribution of any pixel to its corresponding sensor is substantially larger than to the other sensors due to the focusing properties of the lens (Fig. 2, Fig. 3). In other words, the lens performs the spatial separation of the scattered fields emanating from the individual pixels of the discretized contrast source w and routes these fields predominantly to their corresponding focal points.

The full-rank matrix $\mathbf{F}^{\mathcal{S}}$ indicates well-posedness of the underlying inverse scattering problem formulation. In [20], it was shown that such well-posed formulation of the inverse problem allows for its direct solution in analogous manner to the solution of the forward scattering problem. For comparison, in Fig. 4 we present the singular values plot of the matrix $\mathbf{G}^{\mathcal{S}}$ resulting from the discretization of the operator $\mathcal{G}^{\mathcal{S}}$ in the case when the imaging experiment is staged in the homogeneous background media and the matrix $\mathbf{F}^{\mathcal{S}}$ resulting from the discretization of the operator $\mathcal{F}^{\mathcal{S}}$ in the case when the imaging experiment is conducted in the presence of the focusing media (Fig. 3). The matrix $\mathbf{G}^{\mathcal{S}}$ is seen to be rank deficient and hence not being able to produce a unique solution. It is a manifestation of the ill-posedness in the pertinent formulation of the inverse scattering problem in the non-focused imaging setup.

E. CSI ALGORITHM IN FOCUSING MEDIA

The inverse source problem (5) can be solved iteratively as a non-linear optimization problem using the CSI algorithm [10], [14]. The cost-functional $\mathbb{F}$ combines two types
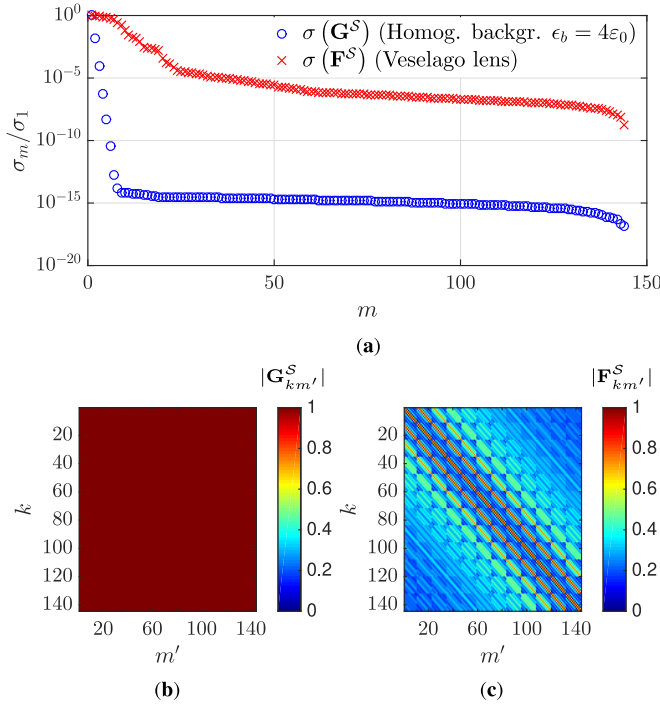
FIGURE 4. (a) Singular values of the matrices $\mathbf{G}^{\mathcal{S}}$ (11) and $\mathbf{F}^{\mathcal{S}}$ (13) resulting from the discretization of the corresponding operators (2), (6) in the imaging experiments staged in the homogeneous background $\epsilon_b = 4\epsilon_0$ and focusing media, respectively. (b) Depiction of the rank-deficient matrix $\mathbf{G}^{\mathcal{S}}$ that has the condition number $\approx 10^{16}$. (c) Depiction of the full-rank matrix $\mathbf{F}^{\mathcal{S}}$ that has the condition number $\approx 10^8$. Imaging domain discretization, sensor locations and media parameters correspond to the numerical experiment depicted in Fig. 5.

of errors: mismatch in the scattered field at sensor locations ρ for the current guess of the contrast sources $\widetilde{w}$ given by

$$\rho_j(\boldsymbol{\rho}) = E^{\mathrm{sc}}(\boldsymbol{\rho}|j) - \mathcal{F}^{\mathcal{S}}\{\boldsymbol{\rho}, \widetilde{w}(\boldsymbol{\rho}'|j)\}, \quad \rho \in \mathcal{S} \quad (14)$$

and mismatch in the total field inside the imaging domain $\mathcal{D}$ for the current guess of the contrast sources $\widetilde{w}$ and contrast function $\widetilde{\chi}$ given by

$$r_j(\boldsymbol{\rho}) = \widetilde{\chi}(\boldsymbol{\rho}')\Big(E^{\mathrm{in}}(\boldsymbol{\rho}'|j) + \mathcal{F}^{\mathcal{D}}\{\boldsymbol{\rho}, \widetilde{w}(\boldsymbol{\rho}'|j)\}\Big) - \widetilde{w}(\boldsymbol{\rho}'|j),$$
$$\rho \in \mathcal{D}, \quad (15)$$

where j is the excitation number, $j = 1, \ldots, J$.

The mismatches ρ_j and r_j in (14) and (15) are often called errors in the data equation and domain equation [15] and have the meaning of how well the current guess of the contrast function $\widetilde{\chi}$ and contrast sources $\widetilde{w}$ satisfy (4) and (5), respectively. By introducing the following normalizations,

$$\eta^{\mathcal{S}} = \left(\sum_{j=1}^{J} \left\|E^{\mathrm{sc}}(\boldsymbol{\rho}|j)\right\|_{\mathcal{S}}^2\right)^{-1},$$

$$\eta^{\mathcal{D}} = \left(\sum_{j=1}^{J} \left\|\widetilde{\chi}(\boldsymbol{\rho}')E^{\mathrm{in}}(\boldsymbol{\rho}'|j)\right\|_{\mathcal{D}}^2\right)^{-1} \quad (16)$$

Algorithm 1 Contrast Source Inversion (CSI) Method [10] in Focusing Media

Inputs: True (measured) field at sensor locations $\underline{E}^{\mathrm{sc}}$, $\underline{E}^{\mathrm{in}}$, incident field inside the imaging domain $\underline{E}^{\mathrm{in},\mathcal{D}}$, discretized operators $\mathbf{F}^{\mathcal{S}}$, and $\mathbf{F}^{\mathcal{D}}$, required relative tolerance *tol*
Output: reconstructed contrast function $\underline{\widetilde{\chi}}$, normalized mismatch at sensors $\delta^{\mathcal{S}}$ and in the domain equation $\delta^{\mathcal{D}}$

1: Calculate initial guess $\underline{\widetilde{w}}^{(0)}$ and $\underline{\widetilde{\chi}}^{(0)}$
2: Calculate $\eta^{\mathcal{S}}$ and $\eta^{\mathcal{D}(0)}$ according to (16)
3: $\underline{\rho}^{(0)} = \underline{E}^{\mathrm{sc}} - \mathbf{F}^{\mathcal{S}} \cdot \underline{\widetilde{w}}^{(0)}$ (14)
4: $\underline{r}^{(0)} = \underline{\widetilde{\chi}}^{(0)} \odot \left(\underline{E}^{\mathrm{in}} + \mathbf{F}^{\mathcal{D}} \cdot \underline{\widetilde{w}}^{(0)}\right) - \underline{\widetilde{w}}^{(0)}$ (15)
5: **for** $n = 1, \ldots, N$ **do**
6: $\quad \underline{g}^{(n)} = -2\Big(\eta^{\mathcal{S}}\mathbf{F}^{\mathcal{S}*} \cdot \underline{\rho}^{(n-1)} +$
$\quad\quad \eta^{\mathcal{D}(n-1)}\left(\underline{r}^{(n-1)} - \mathbf{F}^{\mathcal{D}*} \cdot \underline{\bar{\widetilde{\chi}}}^{(n-1)} \circ \underline{r}^{(n-1)}\right)\Big)$ (18)
7: $\quad \underline{v}^{(n)} = \underline{g}^{(n)} + \dfrac{\left(\underline{g}^{(n)} - \underline{g}^{(n-1)}\right)^* \underline{g}^{(n)}}{\underline{g}^{(n-1)*}\underline{g}^{(n-1)}}\underline{v}^{(n-1)}$
$\quad$ {search direction}
8: $\quad \alpha^{(n)} = \dfrac{-\mathrm{Re}\left(\underline{v}^{(n)*}\underline{g}^{(n)}\right)}{\eta^{\mathcal{S}}\left\|\mathbf{F}^{\mathcal{S}} \cdot \underline{v}^{(n)}\right\|^2 + \eta^{\mathcal{D}(n-1)}\left\|\underline{v}^{(n)} - \underline{\chi}^{(n-1)} \odot \mathbf{F}^{\mathcal{D}} \cdot \underline{v}^{(n)}\right\|^2}$
$\quad$ {search distance}
9: $\quad \underline{\widetilde{w}}^{(n)} = \underline{\widetilde{w}}^{(n-1)} + \alpha^{(n)}\underline{v}^{(n)}$
10: $\quad \underline{E}^{\mathcal{D}(n)} = \underline{E}^{\mathrm{in},\mathcal{D}} + \mathbf{F}^{\mathcal{D}} \cdot \underline{\widetilde{w}}^{(n)}$
$\quad$ {total field inside $\mathcal{D}$ due to $\underline{\widetilde{w}}^{(n)}$}
11: $\quad \underline{\widetilde{\chi}}^{(n)} = \left(\underline{\widetilde{w}}^{(n)} \odot \underline{\bar{E}}^{\mathcal{D}(n)} \oslash |\underline{E}^{\mathcal{D}(n)}|^2\right)$
12: $\quad \underline{\rho}^{(n)} = \underline{E}^{\mathrm{sc}} - \mathbf{F}^{\mathcal{S}} \cdot \underline{\widetilde{w}}^{(n)}$ (14)
13: $\quad \delta^{\mathcal{S}} = \eta^{\mathcal{S}}\left\|\underline{\rho}^{(n)}\right\|^2$
14: $\quad \delta^{\mathcal{D}} = \eta^{\mathcal{D}}\left\|\underline{r}^{(n)}\right\|^2$
15: $\quad$ **if** $(\delta^{\mathcal{S}} < tol)$ **AND** $(\delta^{\mathcal{D}} < tol)$ **then**
16: $\quad\quad$ **return** $\underline{\widetilde{\chi}}^{(n)}, \delta^{\mathcal{S}}, \delta^{\mathcal{D}}$
17: $\quad$ **else**
18: $\quad\quad \underline{r}^{(n)} = \underline{\widetilde{\chi}}^{(n)} \odot \left(\underline{E}^{\mathrm{in}} + \mathbf{F}^{\mathcal{D}} \cdot \underline{\widetilde{w}}^{(n)}\right) - \underline{\widetilde{w}}^{(n)}$ (15)
19: $\quad\quad$ Update $\eta^{\mathcal{D}(n)}$ according to (16)
20: $\quad$ **end if**
21: **end for**

the cost-functional $\mathbb{F}$ [14] can be written in a compact form, as follows:

$$\mathbb{F}(\chi, w_j) = \eta^{\mathcal{S}}\sum_{j=1}^{J}\left\|\rho_j\right\|_{\mathcal{S}}^2 + \eta^{\mathcal{D}}\sum_{j=1}^{J}\left\|r_j\right\|_{\mathcal{D}}^2. \quad (17)$$

Minimization of the cost-functional $\mathbb{F}$ in (17) via CG method requires the computation of Fréchet derivatives [28] and leads to the following expression for the gradient [14]

$$g_j = \frac{\partial\mathbb{F}(\chi, w_j)}{\partial w_j} = \frac{\partial\mathbb{F}^{\mathcal{S}}(\chi, w_j)}{\partial w_j} + \frac{\partial\mathbb{F}^{\mathcal{D}}(\chi, w_j)}{\partial w_j}$$
$$= -2\Big(\eta^{\mathcal{S}}\mathcal{F}^{\mathcal{S}*}\{\boldsymbol{\rho}', \rho_j\} + \eta^{\mathcal{D}}\left(r_j - \mathcal{F}^{\mathcal{D}*}\{\boldsymbol{\rho}', \bar{\widetilde{\chi}}r_j\}\right)\Big), (18)$$

where $\bar{\widetilde{\chi}}$ denotes the complex-conjugate, $\mathcal{F}^{\mathcal{S}*}$ and $\mathcal{F}^{\mathcal{D}*}$ are the adjoint operators to $\mathcal{F}^{\mathcal{S}}$ and $\mathcal{F}^{\mathcal{D}}$ defined in (6). In (18),
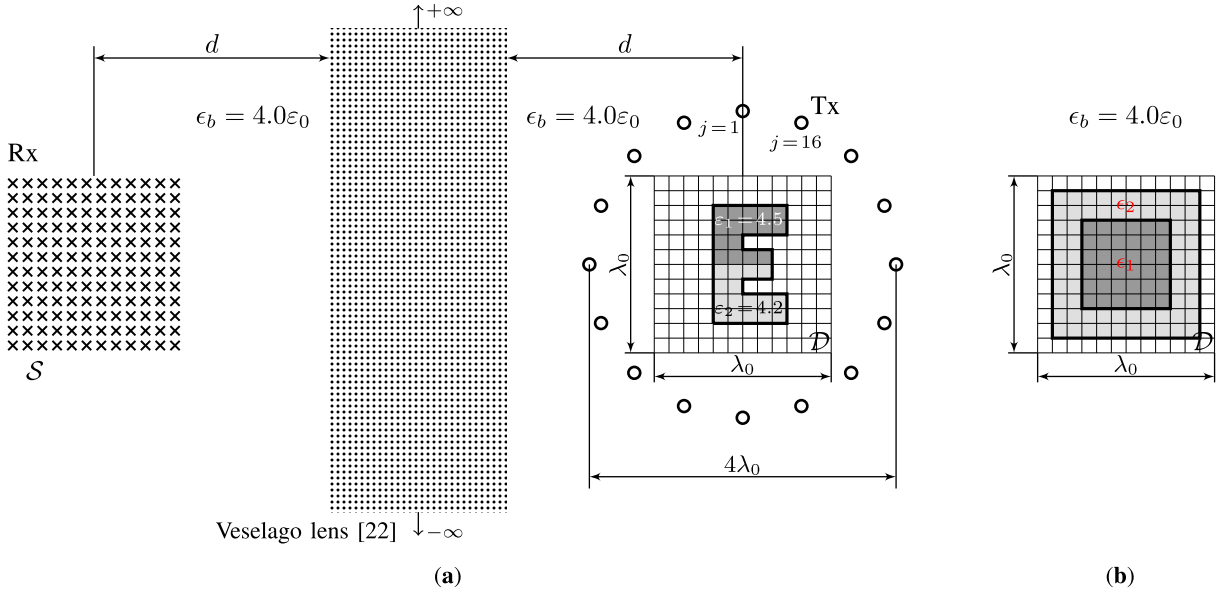
FIGURE 5. (a) Experiment setup for the CSI inversion in the presence of the Veselago lens. The observation points (Rx) are positioned in the lens focal points of the pixels discretizing the imaging domain $\mathcal{D}$ for the *'E'-shaped object*. The interrogating field is produced by point sources (Tx) uniformly distributed around the imaging domain. (b) Depiction of the *2-layer square object* used in the validation of the modified CSI algorithm.

$\mathbb{F}^{\mathcal{S}}$ is the component of the functional responsible for the mismatch in the scattered field at sensor locations ρ (14), and $\mathbb{F}^{\mathcal{D}}$ component is the mismatch in the domain equation (4) for the current guess of the contrast χ.

The CSI algorithm in the homogeneous background media with wavenumber k_b can be formulated by changing operators $\mathcal{F}^{\mathcal{S}}$, $\mathcal{F}^{\mathcal{D}}$, $\mathcal{F}^{\mathcal{S}*}$, and $\mathcal{F}^{\mathcal{D}*}$ with scattering operators $\mathcal{G}^{\mathcal{S}}$, $\mathcal{G}^{\mathcal{D}}$, $\mathcal{G}^{\mathcal{S}*}$ and $\mathcal{G}^{\mathcal{D}*}$ defined in (2). The detailed derivation of the CSI algorithm and update parameters for CG method are presented in [10]. In this paper, we give the general pseudo-code for the CSI (Algorithm 1) using Polak-Ribiere search directions [36] for $J = 1$ excitation. Our algorithm formulation is slightly different from [14], as operators are generalized to allow for the inversion in the focusing media, and the stopping criteria is based not only on the mismatch at the sensor locations ρ (14), but also on the mismatch in the domain equation r (15). In Algorithm 1, * is used to denote the conjugate transpose and $\odot$ is the entrywise Hadamard product [37] and $\oslash$ is the entrywise division.

F. INITIAL GUESS

The presence of the focusing media and its proper positioning with respect to the imaging domain $\mathcal{D}$ and sensor locations $\mathcal{S}$ has been observed to have a profound positive impact not only on the spectral properties of the discretized operators, but also on the quality of the initial guess in the solution. The CSI algorithm is initiated by estimation of the contrast source value function $\widetilde{w}^{(0)}$ using the back-propagation relationship between the true scattered field measured at the sensor locations $\underline{E}^{\mathrm{sc}}$ and the contrast sources [19]

$$\widetilde{w}^{(0)} = \mathbf{F}^{\mathcal{S}*} \cdot \underline{E}^{\mathrm{sc}}, \tag{19}$$

followed by the estimation of the total field $\underline{E}^{\mathcal{D}(0)}$ in the imaging domain using discretized operator $\mathbf{F}^{\mathcal{D}}$ acting on the estimated contrast source $\widetilde{w}^{(0)}$

$$\underline{E}^{\mathcal{D}(0)} = \mathbf{F}^{\mathcal{D}} \cdot \widetilde{w}^{(0)}. \tag{20}$$

Fig. 10 and Fig. 11 show the initial guess for the contrast χ_0 obtained in the homogeneous background media ($\epsilon_b = 4\epsilon_0$) and in the presence of the lens for the 'E'-shaped inhomogeneous object. It's not difficult to see that a substantially higher accuracy estimate of the imaged object is obtained when the initial guess search is aided by the focusing environment of the lens.

III. NUMERICAL RESULTS

To validate a modification of the CSI algorithm accommodating for the presence of the focusing media, we perform numerical reconstruction of the relative electric permittivity distribution (1) for two different objects. The first one is a *2-layer square object* consisting of the denser core scatterer of a square cross-section centered at the origin and having side length of $0.9\lambda_0$ and the layer of a square cross-section tightly surrounding the core scatterer, centered at the origin and having the length of its side of $0.5\lambda_0$ (Fig. 5). The relative permittivity of the core scatterer is ϵ_1, while the relative permittivity of the surrounding square shell is ϵ_2. The second imaged object is a lossless *'E'-shaped object'* composed of two different materials with relative permittivity $\varepsilon_1 = 4.2$ and $\varepsilon_2 = 4.5$ depicted in Fig. 5. The loss (imaginary part of ϵ_1 and ϵ_2) for the *2-layer square object* is specified for individual simulations in the caption for Fig. 10, while for lossless simulations, $\epsilon_1 = \varepsilon_1 = 4.5$ and $\epsilon_2 = \varepsilon_2 = 4.2$.

In both experiments, the imaging domain of $\lambda_0 \times \lambda_0$ at the 6.77 GHz frequency of the interrogating field is discretized
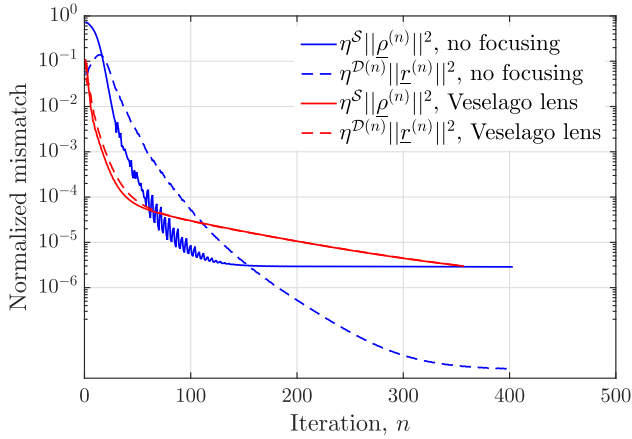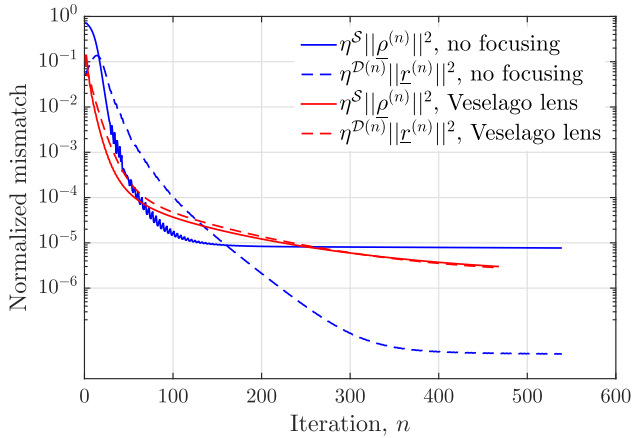
FIGURE 6. Error behavior as a function of CG iterations in the CSI algorithm for the *2-layer square object*. The scattered field error $\eta^{\mathcal{S}} \|\underline{\rho}^{(n)}\|^2$ in the data domain $\mathcal{S}$ and the error $\eta^{\mathcal{D}(n)} \|\underline{r}^{(n)}\|^2$ in the contrast source w in the imaging domain $\mathcal{D}$ are plotted versus the iteration index in CG optimization. The mismatch is depicted for the imaging set up in the homogeneous background ($\epsilon_b = 4\epsilon_0$) and in the focusing media provided by the Veselago lens.

FIGURE 7. Error behavior as a function of CG iterations in the CSI algorithm for the *'E'-shaped object*. The scattered field error $\eta^{\mathcal{S}} \|\underline{\rho}^{(n)}\|^2$ in the data domain $\mathcal{S}$ and the error $\eta^{\mathcal{D}(n)} \|\underline{r}^{(n)}\|^2$ in the contrast source w in the imaging domain $\mathcal{D}$ are plotted versus the iteration index in CG optimization. The mismatch is depicted for both the case of imaging set up in the homogeneous background ($\epsilon_b = 4\epsilon_0$) and in the focusing media provided by the Veselago lens.

FIGURE 8. The error in the reconstructed contrast as a function of CG iterations for the *2-layer square object* in case of the CSI algorithm in the homogeneous background $\epsilon_b = 4\epsilon_0$ and in the presence of the Veselago lens focusing media. The corresponding plots of the sought contrast χ (1) at intermediate and final iteration are given in Fig. 10.

FIGURE 9. The error in the reconstructed contrast as a function of CG iterations for the *'E'-shaped object* in case of the CSI algorithm in the homogeneous background $\epsilon_b = 4\epsilon_0$ and in the presence of the Veselago lens focusing media. The corresponding plots of the sought contrast χ (1) at intermediate and final iteration are given in Fig. 11. To study the possibility of improving the image quality in the homogeneous background CSI algorithm through the emphasis of the contrast source mismatch $\eta^{\mathcal{D}} \|\underline{r}^{(n)}\|^2$ compared to the data mismatch $\eta^{\mathcal{S}} \|\underline{\rho}^{(n)}\|^2$, the cases of nominal weighting coefficient $\eta^{\mathcal{S}}$ as well as cases of reduced contribution of data mismatch into overall error and functional $\mathbb{F}$ (17) $0.5\eta^{\mathcal{S}}$ and $0.1\eta^{\mathcal{S}}$ are considered.

with 144 elements situated on equidistant 12×12 grid of square elements (pixels). To ensure proper focusing properties of the Veselago lens for the particular imaging domain and its discretization, the background material relative electric permittivity and magnetic permeability are taken to be 4 and 1. The relative permittivity and permeability of the Veselago lens are -4 and -0.999999, respectively. Note that the closer the lens relative permeability gets to -1, the more ideal are its focusing properties, and the more challenging becomes the numerical evaluation of its Green's function [24], [32]. The thickness of the lens is 2 m. The interrogating field is produced by a point source located $2\lambda_0$ away from the origin. The properties of the background material with refraction index of 2 as well as material of the superlens with refraction index of -2 are taken to be close to the experimental values of the background medium
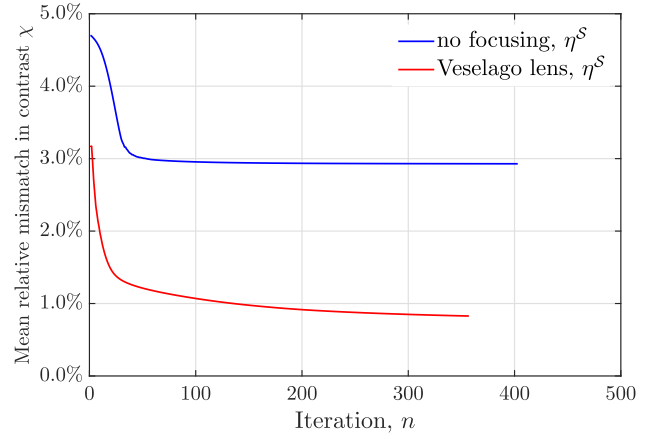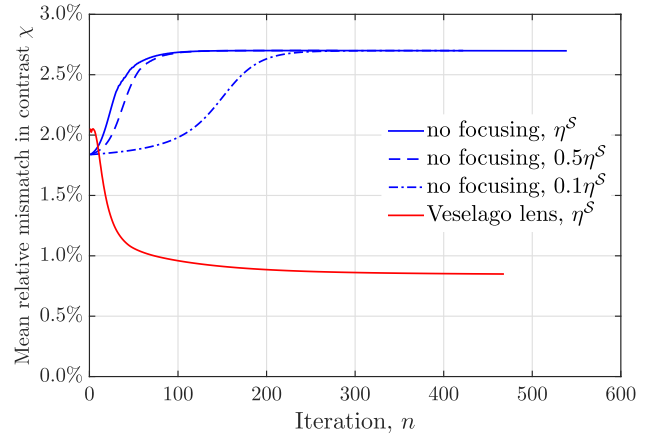
index of refraction 1.925 and the lens index of refraction -1.925 reported in the pioneering experimental demonstration of microwave superlens [26]. In order to image a 2-D object we take a substantially thicker lens, however, than the one reported in [26] where the image of a single point source is reconstructed. The larger thickness of the lens allows for large distance between the lens and the data domain $\mathcal{S}$ and reduces the effect of fringing fields present between the lens and focal spot (see Fig. 2). In practical experimental set ups, the thickness of the lens could be substantially reduced albeit at some loss of image quality.

In both numerical experiments, $J = 16$ different locations of the point source are used to increase the reconstruction quality. The scattered field data used in the proposed
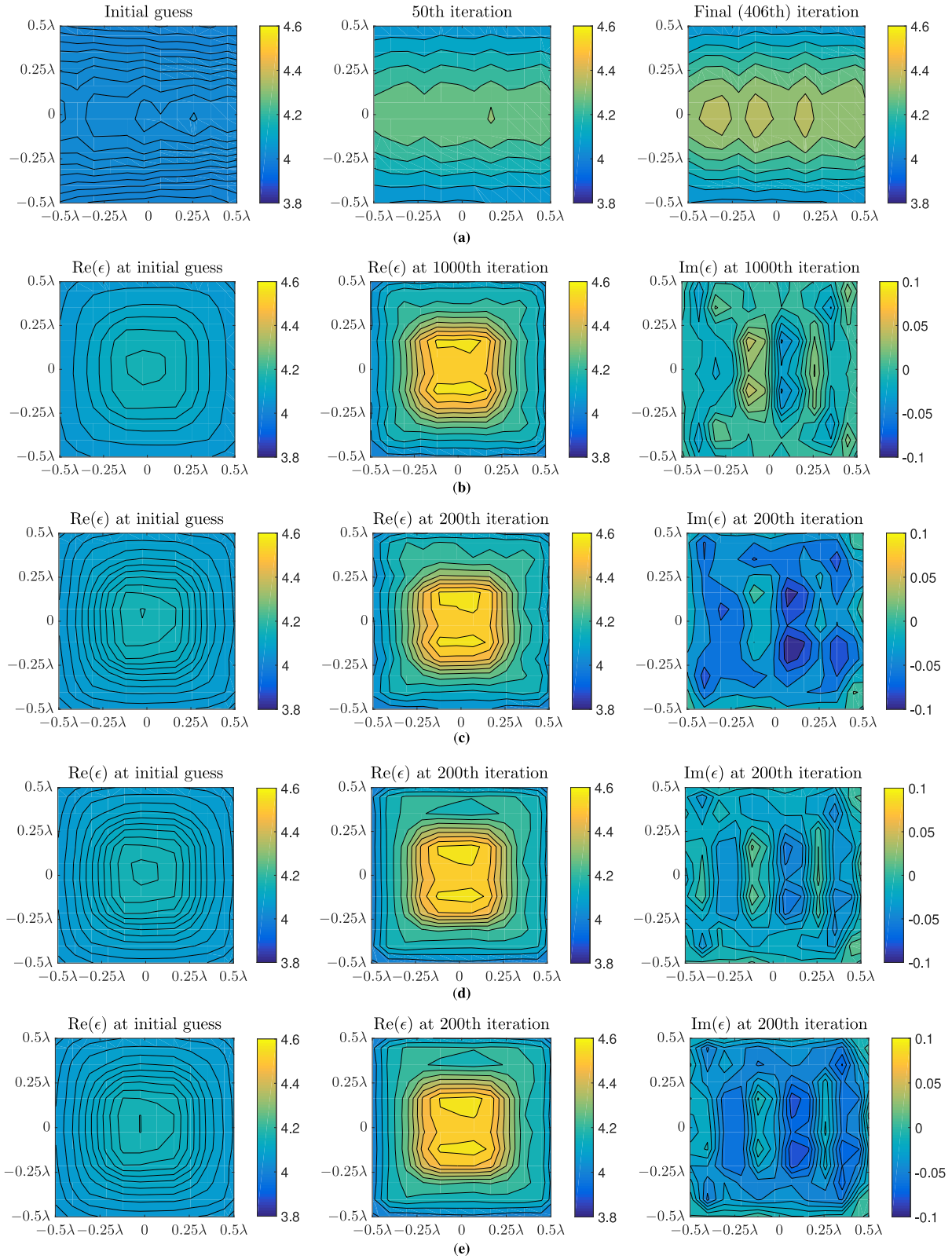
FIGURE 10. Reconstructed relative dielectric permittivity ϵ_{CSI} at different iterations of the CG search for the CSI algorithms in the homogeneous background $\epsilon_b = 4\varepsilon_0$ (a) and focusing media of Veselago lens (b)-(e) for the *2-layer square object* depicted in Fig. 5b: (b) $Im[\epsilon_{CSI}] = 0$, $SNR = \infty$, (c) $Im[\epsilon_{CSI}] = -0.04$, $SNR = 10$, (d) $Im[\epsilon_{CSI}] = -0.02$, $SNR = 33.3$, (e) $Im[\epsilon_{CSI}] = -0.04$, $SNR = 33.3$.

CSI method was generated synthetically via solution of the forward scattering problem for the same object. To avoid the inverse crime and ensure accurate computation of the scattered field at the receiver points, in the forward scattering solution the imaging domain is discretized with 400 pixels.
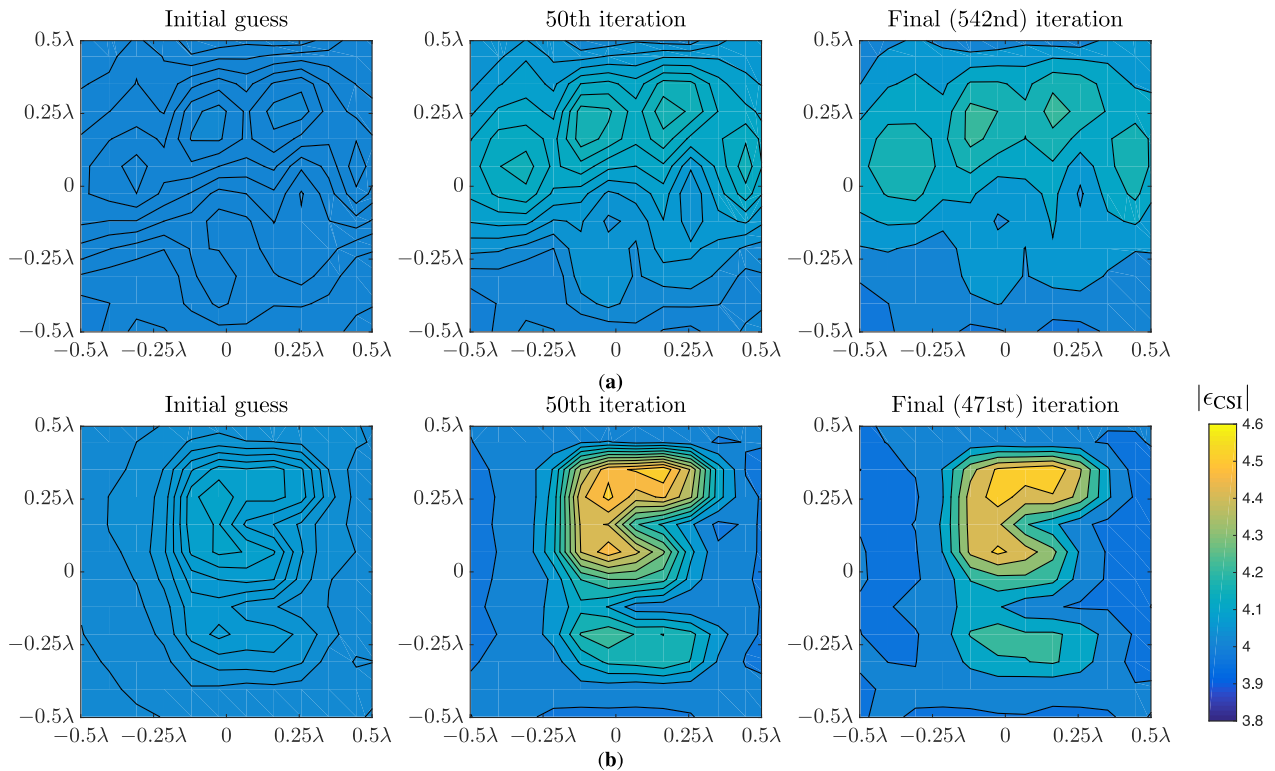
FIGURE 11. Reconstructed relative dielectric permittivity $|\epsilon_{\text{CSI}}|$ at the initial guess, intermediate, and the final iteration of the CG search for the CSI algorithms in the homogeneous background $\epsilon_b = 4\varepsilon_0$ (a) and focusing media of Veselago lens (b) for the *'E'-shaped object*. The imaging set up in focusing media is depicted in Fig. 5a.

Fig. 10 and Fig. 11 show the evolution of the reconstructed permittivity of the *2-layer square object* and *'E'-shaped object*, respectively, over the iteration of the CSI algorithms in the case when the imaging experiment is conducted inside the homogeneous background ($\epsilon_b = 4\varepsilon_0$ and in the case when the focusing media of Veselago lens is present. All the other parameters in the numerical image reconstruction with the CSI algorithm were otherwise the same. The experiments in Fig. 6-9, 11 were conducted in the absence of either noise or loss in the materials (except for non-idealities of the lens). To demonstrate effect of the noise and ability of modified CSI to reconstruct imaginary part of the permittivity additive noise with different signal-to-noise-ratio (SNR) and non-zero conductivity were considered in the cases of 2-layer square object reconstruction in Fig. 10 (c)-(e). Specifically, the sensor locations (i.e., the observation points) remained at the same exactly positions in both experiments. They were positioned to be in a proper correspondence to the locations of the pixels discretizing the imaging domain with respect to the lens' plane of symmetry as depicted in Fig. 5. In the homogeneous background experiment, the lens was removed, however. One can see that while the CSI algorithm in the focusing media consistently improves the image quality as the CG iterations progress, the experiment staged in the homogeneous background did not produce a recognizable image of the object as a result of the CG search for either the *2-layer square* or *'E'-shaped scatterer*.

The mismatches between the true scattered field and the scattered field produced by the contrast source approximation in the conventional CSI algorithm and its proposed modification due to the presence of the focusing media are shown in Fig. 6 for the case of the *2-layer square object* and in Fig. 7 for the case of the *'E'-shaped object*. The CG iterations in the homogeneous background CSI algorithm showed similar convergence, prior to flattening out of the sensor mismatch as a function of the iteration count and its stagnation. However, as it can be seen from Fig. 10 and Fig. 11 the reconstructed permittivity remained far in value from the true one at every iteration of the CG search process. This is due to manifestation of the ill-posedness associated with the formulation of the inverse source problem in the absence of the focusing media. The non-uniqueness of the solution results in the existence of multiple contrast source functions w which can produce the same scattered field values at the sensor locations. In the CSI imaging experiment conducted in the focusing media, the ill-posedness of the inverse problem is eliminated. As a result, only one unique and true distribution of the contrast source w can produce the correct values of the scattered field at the sensor locations. Thus, the contrast w during the CG iterative process is seen to converge to its true values when the focusing media is present, and the underlying formulation of the inverse problem is well-posed.

The behavior of the error in the reconstructed contrast is shown in Fig. 8 for the *2-layer square object* and in Fig. 9 for the *'E'-shaped object*. The error behavior in the sought

contrast over iterations is very different for the case of the imaging experiment staged in the homogeneous background and in the presence of the Veselago lens. In the case of the *'E'-shaped object*, the error in the reconstructed contrast is growing in the process of CG iterative search when the focusing media of the lens is absent. While such behavior should be possible to avoid in principle by increasing the contribution into the functional due to the mismatch in the contrast source by reducing the contribution of data error $\eta^{\mathcal{S}} \| \underline{\rho}^{(n)} \|^2$ into the functional (17), we have found that even in the case of substantial dominance of the contrast source term $\eta^{\mathcal{D}} \| \underline{r}^{(n)} \|^2$ in the functional the error in the contrast still grows over CG iterations as demonstrated in Fig. 9.

The CSI algorithm has been known to successfully produce images in the absence of the focusing media [14], [15]. The reason the reconstruction results of poor quality are obtained in homogeneous background imaging set up are due to the following two factors. First, the location of the sensors in the homogeneous background imaging set-up is sub-optimal for the image reconstruction. Specifically, the observation points are located at the points where they would be best positioned if the lens was present. Optimal positioning of the observation points in homogeneous background CSI algorithm, however, is all around the object as there is no preferential direction to where the field is scattered by the object. Note, however, that in our experiments the positioning of the receive points was intentionally preserved to be the same as in the imaging experiments involving the lens in order to identify the difference in the quality of image reconstruction achieved due to the presence of the focusing media. Second, the imaging experiments in homogeneous media are typically conducted at multiple frequencies [14], [15] in order to obtain recognizable images in the CSI algorithm. The results of the image reconstruction in homogeneous background in this work are conducted at one frequency of the interrogating field which is the same frequency as the frequency used in the CSI image reconstruction when the lens was present.

IV. CONCLUSION

The paper describes a modification of the Contrast Source Inversion (CSI) algorithm which conducts image reconstruction of an object from its scattered electromagnetic field in the presence of a focusing media. The focusing media is formed by the Veselago lens which is properly positioned with respect to the object and the sensor locations at which the scattered field data is collected. Such set up of the imaging experiment in the presence of the focusing media is shown to eliminate the ill-posedness of the inverse scattering problem formulation and to greatly improve the accuracy and robustness of the CSI algorithm. The improvements of the proposed modified CSI algorithm are demonstrated in the numerical image reconstruction from the synthetic scattered field data produced by inhomogeneous objects of complex shape.

REFERENCES

[1] E. C. Fear, S. C. Hagness, P. M. Meaney, M. Okoniewski, and M. A. Stuchly, "Enhancing breast tumor detection with near-field imaging," *IEEE Microw. Mag.*, vol. 3, no. 1, pp. 48–56, Mar. 2002.

[2] S. Kharkovsky and R. Zoughi, "Microwave and millimeter wave non-destructive testing and evaluation—Overview and recent advances," *IEEE Instrum. Meas. Mag.*, vol. 10, no. 2, pp. 26–38, Apr. 2007.

[3] D. M. Sheen, D. L. McMakin, and T. E. Hall, "Three-dimensional millimeter-wave imaging for concealed weapon detection," *IEEE Trans. Microw. Theory Tech.*, vol. 49, no. 9, pp. 1581–1592, Sep. 2001.

[4] G. Roqueta, L. Jofre, and M. Feng, "Microwave non-destructive evaluation of corrosion in reinforced concrete structures," in *Proc. 5th Eur. Conf. Antennas Propag. (EUCAP)*, Rome, Italy, Apr. 2011, pp. 787–791.

[5] W. R. Stone, *Remote Sensing of the Earth's Surfaces*. New York, NY, USA: Wiley, 1999.

[6] L. B. Conyers and D. Goodman, *Ground-Penetrating Radar: An Introduction for Archaeologists*. London, U.K.: AltaMira Press, 1997.

[7] L. Li, W. Zhang, and F. Li, "Derivation and discussion of the SAR migration algorithm within inverse scattering problem: theoretical analysis," *IEEE Trans. Geosci. Remote Sens.*, vol. 48, no. 1, pp. 415–422, Jan. 2010.

[8] D. J. Daniels, *Ground Penetrating Radar*, 2nd ed. Herts, U.K.: IET, 2004.

[9] M. Soumekh, *Synthetic Aperture Radar Signal Processing*, 1st ed. New York, NY, USA: Wiley, 1999.

[10] P. M. van den Berg and R. E. Kleinman, "A contrast source inversion method," *Inverse Probl.*, vol. 13, no. 6, pp. 1607–1620, Dec. 1997.

[11] W. C. Chew and Y. M. Wang, "Reconstruction of two-dimensional permittivity distribution using the distorted Born iterative method," *IEEE Trans. Med. Imag.*, vol. 9, no. 2, pp. 218–225, Jun. 1990.

[12] C. Gilmore, "Towards an improved microwave tomography system," Ph.D. dissertation, Dept. Elect. Comput. Eng., Univ. Manitoba, Winnipeg, MB, Canada, 2009.

[13] P. Mojabi, "Investigation and development of algorithms and techniques for microwave tomography," Ph.D. dissertation, Dept. Elect. Comput. Eng., Univ. Manitoba, Winnipeg, MB, Canada, 2010.

[14] A. Abubakar, W. Hu, P. M. van den Berg, and T. M. Habashy, "A finite-difference contrast source inversion method," *Inverse Probl.*, vol. 24, no. 6, pp. 65004–650021, Dec. 2008.

[15] A. Zakaria and J. LoVetri, "The finite-element method contrast source inversion algorithm for 2D transverse electric vectorial problems," *IEEE Trans. Antennas Propag.*, vol. 60, no. 10, pp. 4757–4765, Oct. 2012.

[16] P. C. Hansen, *Rank-Deficient and Discrete Ill-Posed Problems*. Philadelphia, PA, USA: SIAM, Jan. 1998.

[17] A. N. Tikhonov and V. Y. Arsenin, *Solution of Ill-posed Problems*. New York, NY, USA: Halsted Press, 1977.

[18] A. N. Tikhonov, A. V. Goncharsky, V. V. Stepanov, and A. G. Yagola, *Numerical Methods for the Solution of Ill-Posed Problems*. Dordrecht, The Netherlands: Springer, 1995, doi: 10.1007/978-94-015-8480-7.

[19] M. Oristaglio and H. Blok, *Wavefield Imaging and Inversion in Electromagnetics and Acoustics*, TU Delft, Delft, The Netherlands, 1995.

[20] V. Okhmatovski, J. Aronsson, and L. Shafai, "A well-conditioned non-iterative approach to solution of the inverse problem," *IEEE Trans. Antennas Propag.*, vol. 60, no. 5, pp. 2418–2430, May 2012.

[21] V. Okhmatovski, M. J. Feroj, and L. Shafai, "On use of inhomogeneous media for elimination of ill-posedness in the inverse problem," *IEEE Antennas Wireless Propag. Lett.*, vol. 17, no. 5, pp. 857–860, 2018.

[22] V. G. Veselago, "The electrodynamics of substances with simultaneously negative values of ϵ and μ," *Soviet Phys. Uspekhi*, vol. 10, no. 4, pp. 509–514, 1968.

[23] J. B. Pendry, "Negative refraction makes a perfect lens," *Phys. Rev. Lett.*, vol. 85, no. 18, pp. 3966–3969, Oct. 2000.

[24] S. E. Bankov, "Analytic study of electromagnetic-field focusing by a Veselago lens," *J. Commun. Technol. Electron.*, vol. 54, no. 2, pp. 123–133, Mar. 2009.

[25] J. B. Pendry and D. R. Smith, "The quest for the superlens," *Sci. Amer.*, vol. 295, pp. 60–67, Jul. 2006.

[26] A. Grbic and G. V. Eleftheriades, "Overcoming the diffraction limit with a planar left-handed transmission-line lens," *Phys. Rev. Lett.*, vol. 92, Mar. 2004, Art. no. 117403.

[27] N. Fang, H. Lee, C. Sun, and X. Zhang, "Sub–diffraction-limited optical imaging with a silver superlens," *Science*, vol. 308, no. 5721, pp. 534–537, 2005.

[28] V. P. Kantorovich and G. P. Akilov, *Functional Analysis*, 2nd ed. New York, NY, USA: Pergamon, 1982.

[29] A. Menshov and V. Okhmatovski, "Microwave imaging with contrast source inversion method in focusing media," in *Proc. IEEE MTT-S Int. Conf. Numer. Electromagn. Multiphys. Model. Optim.*, Ottawa, ON, Canada, Aug. 2015, pp. 1–3.

[30] M. Born and E. Wolf, *Principles of Optics*, 7th ed. Cambridge, U.K.: Cambridge Univ. Press, 1999.

[31] J. Fostier and F. Olyslager, "Full-wave electromagnetic scattering at extremely large 2-D objects," *Electron. Lett.*, vol. 45, no. 5, p. 245, Feb. 2009.

[32] J. Aronsson and V. Okhmatovski, "Comparison of numerical approaches to the evaluation of Veselago lens' Green's function," in *Proc. IEEE Int. Symp. Antennas Propag.*, Spokane, WA, USA, Jul. 2011, pp. 1519–1521.

[33] R. Harrington, *Field Computation by Moment Methods*. New York, NY, USA: Wiley, 1993.

[34] W. H. Press, S. A. Teukolsky, W. T. Vetterling, and B. P. Flannery, *Numerical Recepies: The Art of Scientific Computing*, 3rd ed. Cambridge, U.K.: Cambridge Univ. Press, 2007.

[35] D. R. Wilton, S. M. Rao, A. W. Glisson, D. H. Schaubert, O. M. Al-Bundak, and C. M. Butler, "Potential integrals for uniform and linear source distributions on polygonal and polyhedral domains," *IEEE Antennas Propag. Mag.*, vol. 32, no. 3, pp. 276–281, Mar. 1984.

[36] E. Polak and G. Ribiere, "Note sur la convergence de méthodes de directions conjuguées," *Modélisation Mathématique et Analyse Numérique*, vol. 3, no. 16, pp. 35–43, 1969.

[37] R. A. Horn and C. R. Johnson, *Matrix Analysis*, 2nd ed. Cambridge, U.K.: Cambridge Univ. Press, 2012.

VLADIMIR I. OKHMATOVSKI (Senior Member, IEEE) was born in Moscow, Russia, in 1974. He received the M.S. degree (with Distinction) in radiophysics and the Ph.D. degree in antennas and microwave circuits from the Moscow Power Engineering Institute, Moscow, in 1996 and 1997, respectively.

In 1997, he joined the Radio Engineering Department, Moscow Power Engineering Institute, as an Assistant Professor. He was a Postdoctoral Research Associate with the National Technical University of Athens from 1998 to 1999, and with the University of Illinois at Urbana-Champaign from 1999 to 2003. From 2003 to 2004, he was with the Department of Custom Integrated Circuits, Cadence Design Systems, as a Senior Member of Technical Staff, and from 2004 to 2008, as an independent consultant. In 2004, he joined the Department of Electrical and Computer Engineering, University of Manitoba, Winnipeg, MB, Canada, where he is currently a Full Professor. His research interests are the fast algorithms of electromagnetics, high-performance computing, modeling of interconnects, and inverse problems.

Dr. Okhmatovski was the recipient of 2017 Intel Corporate Research Council Outstanding Researcher Award, the 1995 Scholarship of the Government of Russian Federation, and the 1996 Scholarship of the President of the Russian Federation. He was also the recipient of the 1996 Best Young Scientist Report of the VI International Conference on Mathematical Methods in Electromagnetic Theory. He was also a co-recipient of the Best Paper Award of the 3rd Electronic Packaging Technology Conference in 2001 and Outstanding ACES Journal Paper Award in 2007. He is a Registered Professional Engineer in the Province of Manitoba, Canada.

ANTON MENSHOV (Member, IEEE) was born in Kovrov, Russia, in 1988. He received the B.S. degree in automatics and management from the Moscow Institute of Electronic Technology, Moscow, Russia, in 2010, and the M.Sc. degree in electrical and computer engineering from the University of Manitoba, Winnipeg, Canada, in 2014. He is the Vice President of Engineering with CEMWorks, Inc. His current research interest are in fast algorithms for computational electromagnetics and inverse problems.